

RESEARCH PAPER

# *Operando* Synchrotron Studies of Inhomogeneity during Anode-Free Plating of Li Metal in Pouch Cell Batteries

To cite this article: Monty R. Cosby *et al* 2022 *J. Electrochem. Soc.* **169** 020571

View the [article online](#) for updates and enhancements.



## Operando Synchrotron Studies of Inhomogeneity during Anode-Free Plating of Li Metal in Pouch Cell Batteries

Monty R. Cosby,<sup>1,2,=</sup> Gia M. Carignan,<sup>1,2,=,a</sup> Zhuo Li,<sup>1,2</sup> Corey M. Efav,<sup>3</sup> Charles C. Dickerson,<sup>3</sup> Liang Yin,<sup>4</sup> Yang Ren,<sup>4</sup> Bin Li,<sup>3</sup> Eric J. Dufek,<sup>3</sup> and Peter G. Khalifah<sup>1,2,z</sup>

<sup>1</sup>Department of Chemistry, Stony Brook University, Stony Brook, New York 11794-3400, United States of America

<sup>2</sup>Chemistry Division, Brookhaven National Laboratory, Upton, New York 11973, United States of America

<sup>3</sup>Energy Storage and Electric Transportation Department, Idaho National Laboratory, Idaho Falls, Idaho 83415, United States of America

<sup>4</sup>X-ray Science Division, Advanced Photon Source, Argonne National Laboratory, Lemont, Illinois, 60439, United States of America

*Operando* synchrotron X-ray diffraction (XRD) studies have not previously been used to directly characterize Li metal in standard batteries due to the extremely weak scattering from Li atoms. In this work, it is demonstrated the stripping and plating of Li metal can be effectively quantified during battery cycling in appropriately designed synchrotron XRD experiments that utilize an anode-free battery configuration in which a Li-containing cathode material of LiNi<sub>0.6</sub>Mn<sub>0.2</sub>Co<sub>0.2</sub>O<sub>2</sub> (NMC622) is paired with a bare anode current collector consisting of either Cu metal (Cu/NMC) or Mo metal (Mo/NMC). In this configuration, it is possible to probe local variations in the deposition and stripping of Li metal with sufficient spatial sensitivity to map the inhomogeneity in pouch cells and to follow these processes with sufficient time resolution to track state-of-charge-dependent variations in the rate of Li usage at a single point. For the Cu/NMC and Mo/NMC batteries, it was observed that the initial plating of Li occurred in a very homogeneous manner but that severe macroscopic inhomogeneity arose on a mm-scale during the subsequent stripping of Li, contrasting with the conventional wisdom that the greatest challenges in Li metal batteries are associated with Li deposition. © 2022 The Electrochemical Society ("ECS"). Published on behalf of ECS by IOP Publishing Limited. [DOI: 10.1149/1945-7111/ac5345]

Manuscript submitted December 20, 2021; revised manuscript received January 26, 2022. Published February 28, 2022. *This paper is part of the JES/JSS Joint Focus Issue In Honor of John Goodenough: A Centenarian Milestone.*

Supplementary material for this article is available [online](#)

Batteries play an essential role in a wide variety of high-tech applications that are central to modern society, including mobile electronic devices and automobiles.<sup>1,2</sup> With the ongoing transition to electric vehicles, the need for batteries with high energy densities is greater than ever before.<sup>3,4</sup> Lithium metal batteries have been shown to be capable of delivering much higher energy densities than commonly used Li-ion battery technologies.<sup>5</sup> However, there are also serious challenges associated with the use of highly reactive Li metal, and as a result, batteries utilizing this technology have known limitations in their safety and lifetime.<sup>6–10</sup>

Previous work has shown that the lifetime limitations of Li metal batteries are closely linked to the formation of so-called “dead” Li, which is inactivated Li that is unable to contribute to the energy storage of the cell.<sup>11</sup> Intriguingly, it has been shown that the loss of available Li predominantly occurs not through chemical oxidation or reactions of Li metal, but instead through the loss of electronic accessibility to small particles of Li metal that become disconnected from the bulk Li metal substrate.<sup>7</sup> The amount of inactive Li gradually increases with cycling and causes particularly severe limitations in the battery lifetime when cells are built using a minimal excess of Li metal, as is necessarily the case for commercial applications.

Given the importance of dead Li in limiting the performance of Li metal batteries, it is critical to develop methods for understanding the processes that lead to its formation during the cycling of batteries. Although a variety of methods have been developed to study Li metal in the context of electrochemical cells, these efforts have generally been qualitative rather than quantitative.<sup>12,13</sup> Past efforts to quantify the amount of dead Li in Li metal batteries—whether electrochemical<sup>14,15</sup> or chemical<sup>16–18</sup>—have only done so for the cell as a whole and have had limited time resolution. There is presently an unmet need for an advanced characterization technique that can follow the behavior of Li metal with both temporal and

spatial resolution in standard cell geometries commonly used for laboratory testing and/or industrial applications.

Synchrotron X-ray diffraction (XRD) techniques have previously been used to precisely follow changes in battery cathodes during electrochemical cycling.<sup>19</sup> While synchrotron XRD studies have conventionally been used to follow time-dependent changes at a single point (0D), they have more recently shown to be capable of following spatially-dependent changes in batteries during cycling in 1D depth profiling experiments,<sup>20,21</sup> in 2D lateral mapping experiments,<sup>22,23</sup> and even in 3D tomographic mapping studies.<sup>24–26</sup> However, similar experiments to follow changes in Li metal anodes have not been carried out due to the many challenges involved in Li quantification.

It has long been recognized that X-ray scattering from Li ions is exceptionally weak due to the small number of electrons around the Li nucleus. This weak scattering is further exacerbated when whole cells are studied since the intensity of diffraction from other cell components (e.g., cathode, battery housing) is much stronger than that from Li metal. Furthermore, Li metal is typically present in the form of relatively thick and large-grained metal foils that provide a strong baseline response against which the changes that occur during cycling are difficult to resolve. As such, there have been very few prior diffraction studies that have attempted Li quantification in battery systems and these have been done exclusively in an *ex situ* manner in which long data collection times can be used.<sup>27–29</sup> In this work, we demonstrate that by optimizing both the conditions of synchrotron data collection and by utilizing an “anode-free” cell design, it is possible to quantitatively follow the plating and stripping of Li that occurs during electrochemical cycling. Furthermore, this can be done in a spatially resolved manner that allows the local cycling behavior to be compared in regions that do or do not generate substantial amounts of dead Li, providing novel insights into the macroscopic inhomogeneity in Li metal batteries at different times during electrochemical cycling.

### Experimental

Single-layer anode-free pouch cell batteries for *operando* cycling were constructed using a NMC cathode paired with a bare anode current collector of either Cu or Mo, with the two types of cells

<sup>=</sup>These authors contributed equally to this work.

<sup>a</sup>Present address: Department of Chemistry, Rutgers University, Piscataway, New Jersey, 08854, United States of America.

<sup>z</sup>E-mail: [kpete@bnl.gov](mailto:kpete@bnl.gov)

denoted Cu/NMC and Mo/NMC. The pouch cells (40 mm × 60 mm) used single-sided LiNi<sub>0.6</sub>Mn<sub>0.2</sub>Co<sub>0.2</sub>O<sub>2</sub> (NMC622, Targray) as the cathode (areal capacity of 5.5 mAh cm<sup>-2</sup>). The NMC622 cathodes were prepared by Pacific Northwest National Lab using a previously described method.<sup>30</sup> The current collector at the anode side was either copper (12.4 μm, Fisher Scientific) or molybdenum (99.95%, 25 μm, Fisher Scientific). Before pouch cell assembly, current collectors were cleaned by rinsing with dilute sulfuric acid (2 M H<sub>2</sub>SO<sub>4</sub>) for ~20 s, followed by rinsing with first deionized water and then ethanol, and finally drying in the antechamber of the glovebox under vacuum for more than 8 h. Each cell used Celgard® 2325 as separator and 10 g A<sup>-1</sup>h<sup>-1</sup> of electrolyte of 1.2 M lithium hexafluorophosphate (LiPF<sub>6</sub>) in 3:7 (by weight) blend of ethylene carbonate (EC) and ethyl methyl carbonate (EMC) with 10 wt% vinylene carbonate (VC), a commonly used mixture here denoted as Gen. II (density of 1.27 g ml<sup>-1</sup>).

Pouch cells were shipped to the Advanced Photon Source (APS) synchrotron, where they were fixed to a rigid plastic frame (Fig. S1 (available online at [stacks.iop.org/JES/169/020571/mmedia](https://stacks.iop.org/JES/169/020571/mmedia))) with their cathode side facing the detector (chosen due to the slightly reduced overlap between key anode and cathode diffraction peaks in this configuration). *Operando* powder X-ray diffraction measurements were done at the 11-ID-C beamline using a wavelength of 0.1173 Å (105.70 KeV) and a nominal beam size of 0.3 mm by 0.3 mm. Diffraction patterns were collected using a low-noise 2D area detector (Pilatus 2 M CdTe) with dimensions of 1679 × 1475 pixels and a 200 × 200 micron pixel size. The total acquisition time for each pattern was 5 s at sample-to-detector distance of about 870 mm.

During *operando* experiments, the two pristine batteries discussed here (as well as 3 additional cells) were simultaneously charged and discharged using a MACCOR 4300 cycler at a C/10 cycling rate (10 h to fully charge or discharge) calculated based on a theoretical specific capacity of 5.5 mAh cm<sup>-2</sup> (corresponding to a total capacity of 52.25 mAh) and a current density of 0.55 mA cm<sup>-2</sup>. For consistency and timing purposes, charging was carried out only to 80% of the theoretical capacity (41.80 mAh). The measured discharge capacity was 35.83 mAh for the Cu/NMC cell and 34.77 mAh for the Mo/NMC cell, corresponding to a capacity loss of 16.8% and 14.3%, respectively. Measurements were done using two modalities. During cycling, line scan data were repeatedly collected (every 10 min) on each cell for 10 total points (5 × 2 array, with 6 and 10 mm horizontal and vertical step sizes, respectively), with the two rows sequentially accessed in a snake pattern. Additionally, mapping data over 200 points (20 × 10 array on a

2 × 2 mm grid) were collected at a nominal state of charge (SOC) of 0%, 40%, and 80% during each charge (C) and discharge (D) segment after relaxation for 30 min.

The 2D diffraction images were integrated into 1D diffraction patterns using pyFAI.<sup>31</sup> Automated refinements were done using TOPAS version 6 (Bruker AXS)<sup>32</sup> using custom Python scripts for run control. Detector parallax effects were corrected using a 4-term polynomial parameterized through fits to a CeO<sub>2</sub> standard. Sequential refinements were performed on line scan data in the order of data collection. Current collector phases (Al and Cu or Mo) were fit using structure-independent Pawley refinements while structure-based Rietveld fits were used for the active electrode materials (Li and NMC). The strongest Li metal diffraction peak had substantial overlap with an NMC peak at low NMC states of charge, as is illustrated in Fig. S2. To minimize correlations resulting from the overlap that could add uncertainty to the refined amount of Li, it was necessary to optimize the size and strain broadening terms used to fit the NMC peak shape and to constrain the Li lattice parameters to remain near their ideal value (3.4909 ± 0.0075 Å). Input files from sequential refinements at 40% C, 80% C, 40% D, and 0% D (where the number indicates the nominal SOC and the letter indicates charge or discharge) were used as a common template for each of the 200 diffraction patterns comprising the mapping data at each SOC, with the refinement control file for 80% C provided as Supporting Information.

## Results and Discussion

**Designing experiments for Li sensitivity.**—Although the plating and stripping of Li metal is an essential aspect of the cycling of high energy density batteries utilizing Li metal anodes, this process is exceptionally difficult to directly follow during *operando* experiments. These challenges are especially pronounced if one wishes to interrogate the standard battery cell designs used for laboratory testing (coin cells) or industrial applications (pouch cells or cylindrical cells) without severely modifying the cell design to accommodate the measurement technique. Since Li plating and stripping processes are generally expected to be inhomogeneous, it is important that the analysis method be able to track changes not just at one point in the cell but instead provide spatially resolved information for multiple points during cycling.

Previously, *operando* X-ray diffraction methods have been applied to precisely track changes in many cathode materials<sup>33–37</sup> and anode materials<sup>38–42</sup> during the electrochemical cycling of battery cells. The central challenge to the characterization of Li metal by X-ray diffraction is its low scattering power. This is illustrated in Fig. 1 which shows that even when a maximal amount of Li metal has been plated, the height of the most intense diffraction peak from this deposited Li (the 110 peak) is not resolvable on the scale of the diffraction peaks from the other phases in the sample. As a result, prior X-ray diffraction studies on the deposition of Li resulting from battery cycling have generally focused on *ex situ* rather than *operando* studies to enable longer acquisition times that can improve the signal/noise ratio for the data.<sup>29</sup> The one prior *operando* study of Li metal plating and stripping that we are aware of was done using an unconventional cell design that separated the cathode and anode by a few mm,<sup>43</sup> making the diffraction experiment easier but forcing data collection to occur in a cell design quite different from (and not necessarily relevant to) conventional battery designs and not providing spatially resolved information. To the best of our knowledge, there have been no prior *operando* studies quantifying Li deposition and stripping in a standard battery cell in a 2D spatially resolved manner using any technique, diffraction or otherwise.

Although the detection and accurate quantification of X-ray diffraction peaks from Li metal plated during battery cycling is extremely challenging, this goal is potentially achievable through an optimally designed experiment with respect to both the sample and the instrument. Here, the sample scattering was optimized by using

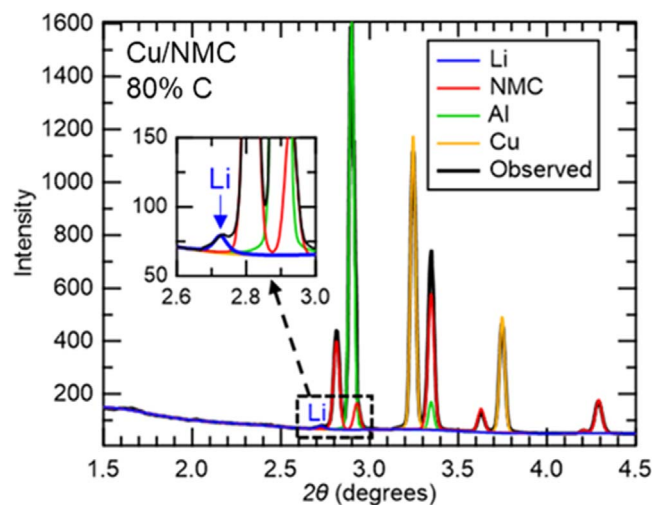


**Figure 1.** Experimental (black) powder diffraction data for a Cu/NMC sample in its 80% C state. The individual peaks for each phase obtained through whole-pattern fitting are superimposed (colors), with the most intense Li metal peak (110 reflection) indicated with a blue arrow.

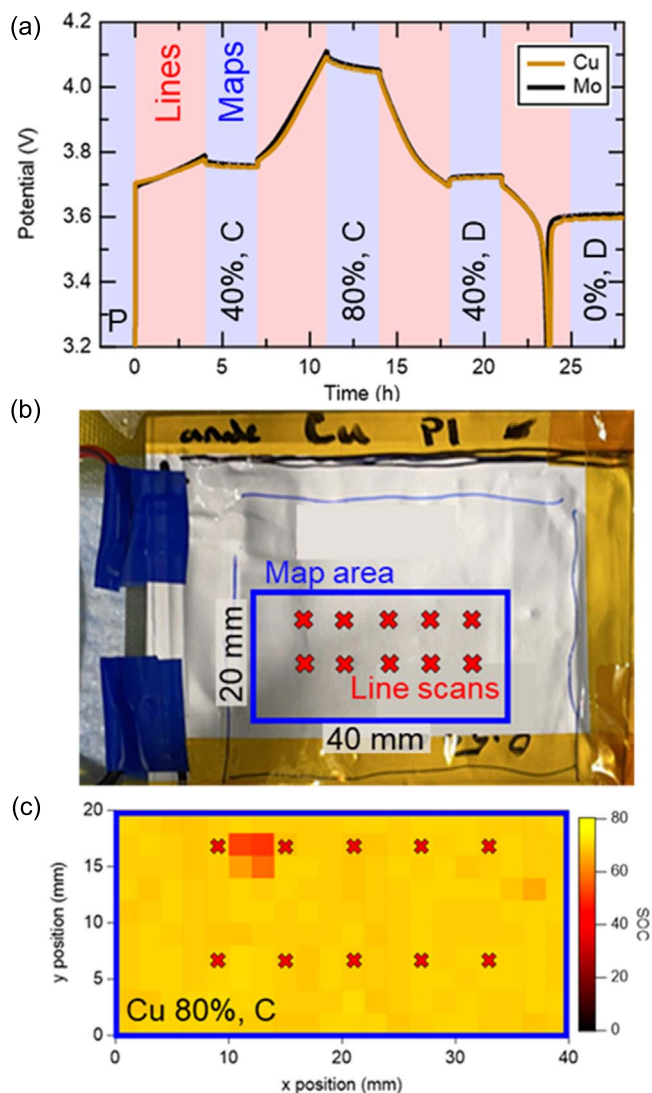


**Figure 2.** Design of experiments. (a) Voltage profiles recorded for the Cu/NMC and Mo/NMC cells during synchrotron experiments, with the data collection modality used at each time indicated by the background color (maps in blue; line scans in red). Time is relative to start of cycling, with the label for each map indicated in black text. (b) Photograph of the mounted cell with the regions of data collection marked with a rectangle for the mapping data and with red crosses for the line scans. (c) A map of the NMC SOC collected for a Cu/NMC cell charged to 80% SOC.

an “anode-free” configuration in which the positive electrode was a bare metal foil of either Cu or Mo, a cell configuration which can lead to maximal energy densities.<sup>44</sup> This avoided the two main problems that occur in typical cells using Li metal foil anodes. First, it is difficult to deconvolute the signal from the Li metal which is initially present from the changes that occur during cycling when Li metal is plated and stripped, especially since the amount of pre-existing Li typically exceeds the amount of deposited Li by an order of magnitude or more. Second, the pre-existing Li metal typically has large grain sizes of hundreds of microns and thus produces diffraction patterns which are spotty rather than having smooth rings, resulting in inadequate sampling and intensities that do not linearly scale with the volume of Li in the beam. On the instrument side, the sensitivity to Li metal depends on the signal/noise ratio, which was optimized both by using an intense synchrotron source and by using a direct photon counting detector that does not suffer from the high read-out noise of conventional synchrotron detectors. In this manner, diffraction patterns suitable for direct Li

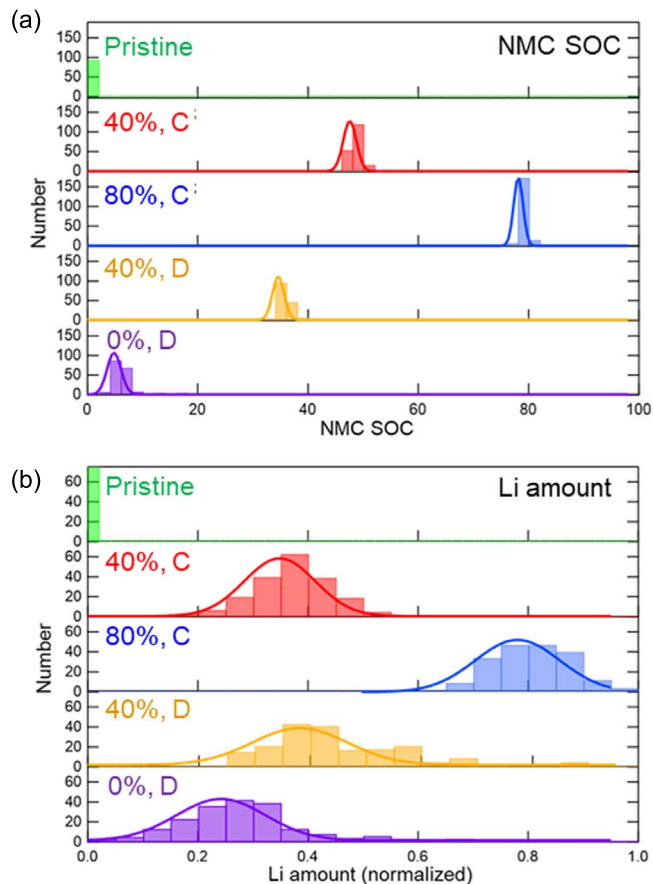


**Figure 3.** Histograms of (a) NMC SOC and (b) normalized Li amount for each map of the Cu/NMC cell. The larger widths of the Li histograms reflect the larger measurement uncertainties. Corresponding data for the Mo/NMC cell is shown in Fig. S4.

quantification could be acquired using total exposure times of about 5 s, a short enough time to permit spatially resolved *operando* high energy lateral mapping (HELM) studies of Li plating and stripping.

**Static studies of in-plane inhomogeneity (maps).**—The spatially-dependent changes that occur first during Li plating (charge segment) and second during Li stripping (discharge segment) were studied for two anode-free single-layer pouch cell batteries. In one battery, the Li was deposited during cycling onto a bare Cu foil used as the current collector while the other instead used a bare Mo foil current collector. During cycling, the cell SOC was increased and decreased by 40% in two steps, with mapping data collected after a half-hour rest at the end of each step. The voltage response during cycling and the timing of the map collection are indicated in Fig. 2a, with blue shading indicating the regions for map collection. As will be discussed in more detail later, complementary line scan data was collected while the battery was cycling in the regions marked in red. The approximate area on the cell that was studied during mapping is indicated with a blue rectangle in Fig. 2b, while a representative 200-pixel map of the NMC state of charge reconstructed from the diffraction data shown in Fig. 2c.

The X-ray diffraction patterns collected at each point were analyzed to follow changes in the battery in two ways, with representative refinements shown in Fig. S3. First, the state of charge of the NMC phase was determined from the refined NMC unit cell volume using methods we have discussed previously.<sup>20</sup> The amount of Li was normalized so that the mean value was 0.80 for the map collected after charging the cell to a SOC of 80%. Second, the amount of Li metal was determined based on the intensity of the 110 diffraction peak of this phase. Histograms of both quantities for each

**Table I. Average NMC SOC and Li amount in maps.**

|               | SOC (%) | Li amount |
|---------------|---------|-----------|
| <b>Cu/NMC</b> |         |           |
| Pristine      | 0.01    | N/A       |
| 40%, C        | 47.8    | 0.36      |
| 80%, C        | 78.9    | 0.80      |
| 40%, D        | 40.5    | 0.44      |
| 0%, D         | 9.17    | 0.28      |
| <b>Mo/NMC</b> |         |           |
| Pristine      | 0.01    | N/A       |
| 40%, C        | 45.3    | 0.60      |
| 80%, C        | 75.9    | 0.85      |
| 40%, D        | 33.0    | 0.50      |
| 0%, D         | 5.24    | 0.09      |

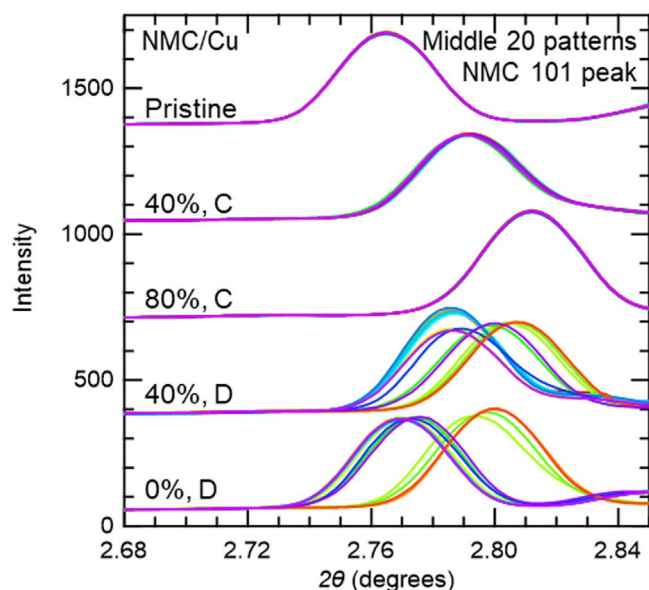


**Figure 4.** Cycling-dependent inhomogeneity in Cu/NMC sample seen directly in powder diffraction data showing the position of the NMC 101 reflection. Twenty patterns are superimposed for each map (data collected for the two columns at the center of the map).

of the 5 maps are presented in Fig. 3 (Cu) and Fig. S4 (Cu/Mo comparison) along with fits to a Gaussian distribution of data points falling within  $2\sigma$  of the mean value, with the statistical distributions reported in Tables I and SI–SIV.

It is expected that both the Li amount and the NMC SOC start at zero in the pristine cell, increase to a maximum value as the cell is charged, and finally drop to a value near zero as the cell is discharged. The histograms clearly indicate that the Li amount quantified from synchrotron diffraction data exhibits the expected behavior, confirming that this technique has sufficient sensitivity to follow the stripping and plating of weakly scattering Li metal even though the maximum amount of deposited Li corresponds to only 21 microns at its theoretical density based on the cathode specific capacity. The widths of the Li amount distributions ( $\sim 10\%$  absolute) are about  $10\times$  larger than the widths of the NMC SOC distributions ( $\sim 1.5\%$  absolute). This width depends both on limitations in the precision of Li metal quantification and on the anode inhomogeneity, though the former is expected to dominate.

The time-dependent inhomogeneity within the cells can be probed by comparing changes in the local performance at different points on the cell. Initial insights were obtained by comparing the diffraction patterns collected at the same 20 pixels of the cell at different times during cycling. As seen in Fig. 4 for the Cu/NMC

cell, the positions of the NMC 101 diffraction peak are nearly identical in all 20 patterns during the cell charge but strongly vary during discharge with local variations in SOC that are about  $\pm 10\%$  absolute. These large variations do not show up well on the scale of the histograms of Fig. 3 because most pixels exhibit the average behavior and also because the non-average pixels are diluted across many more bins than the average pixels. Similar behavior was observed for the Mo/NMC cell (Fig. S5), though with a lesser degree of inhomogeneity. Importantly, this indicates that key problems associated with the use of Li metal manifest during the stripping of Li metal rather than the plating of Li metal, even though the majority of scientific studies on batteries using Li metal focus on remediating problems associated with Li plating (e.g., dendrite formation, low density of deposited Li).

Based on the results of groundbreaking cryo-TEM studies, it has previously been suggested that the formation of inactive or “dead” Li occurs when the stripping of Li from the base of particles electronically disconnects their tips.<sup>45</sup> This behavior was further supported by quantitative studies of inactive Li, which found that it is almost exclusively present as metallic Li<sup>0</sup> rather than ionic Li<sup>+</sup>.<sup>46</sup> If this is indeed the case, then it may be possible to use the present HELM techniques to directly image residual “dead” Li that remains at the end of one complete charge/discharge cycle of an anode-free cell. Furthermore, it should be possible to explore the impact of poor anode performance on nearby regions of the NMC cathode.

Maps comparing the local performance at the pouch cell anode and cathode were therefore prepared. These maps followed both the Li metal amount (anode) and the NMC SOC (cathode) determined from diffraction data. Maps are shown for the Cu/NMC cell and the Mo/NMC cell (Fig. 5). Maps for the pristine cells are shown separately (Fig. S6) as they do not have any deposited Li. Due to the large widths of the Li amount distribution, we have chosen to plot maps of both the absolute amount of Li metal and the amount of Li metal relative to the mean ( $\Delta\text{Li}$ ) of each map, with the latter allowing inhomogeneities to be more clearly resolved. Each map of 200 points sampled an area of  $38\text{ mm} \times 18\text{ mm}$  with  $2 \times 2\text{ mm}$  grid steps. Although the primary goal of these experiments is to understand the behavior of Li, the NMC behavior is discussed first due to the higher precision with which it can be studied.

Looking first at the Cu/NMC maps, the NMC SOC is seen to be quite homogeneous both in the middle (40% C) and at the end (80% C) of the first charge, with only a few of the 200 pixels significantly deviating from the mean values. In contrast, strong inhomogeneity develops by the halfway point of the subsequent discharge (40% D). This inhomogeneity is primarily concentrated in four spots (labeled 1–4) accounting for nearly 25% of the area of the map, with the SOC in these spots lagging the behavior of the rest of the cell by 10%–20%. This extensive NMC inhomogeneity has not been previously seen in our *operando* testing of more conventional Li/NMC cells at the beginning of their lifetime and thus is believed to be a consequence of building the present cell using an anode-free cell design in which there is not a pre-existing reservoir of Li.

Insights into the origin of the anomalous NMC behavior can be gained by examining the distribution of Li metal (measured simultaneously with the NMC SOC) during cell cycling. Although the Li distribution cannot be resolved as precisely as the NMC SOC, it can still be determined from both the Li amount map and the  $\Delta\text{Li}$  maps that each of the 4 spots (1–4) present halfway through discharge and the two spots present at the end of discharge (spots 1 and 2) occur at regions where excess Li metal is present. This indicates that difficulties in stripping Li away from the anode hinder the cycling of the NMC cathode material directly across the separator from these regions on the time scale of these measurements (hours). This is not surprising, as battery cells are typically designed to have fast diffusion on the length scale of the film thickness ( $\sim 50$  microns) rather than on the length scale of the anomalous spots, which are greater by two orders of magnitude ( $\sim 5\text{ mm}$ ). Intriguingly, the length scale of the spots seen here is similar to that seen in our previous mapping experiments probing the failure of Li/

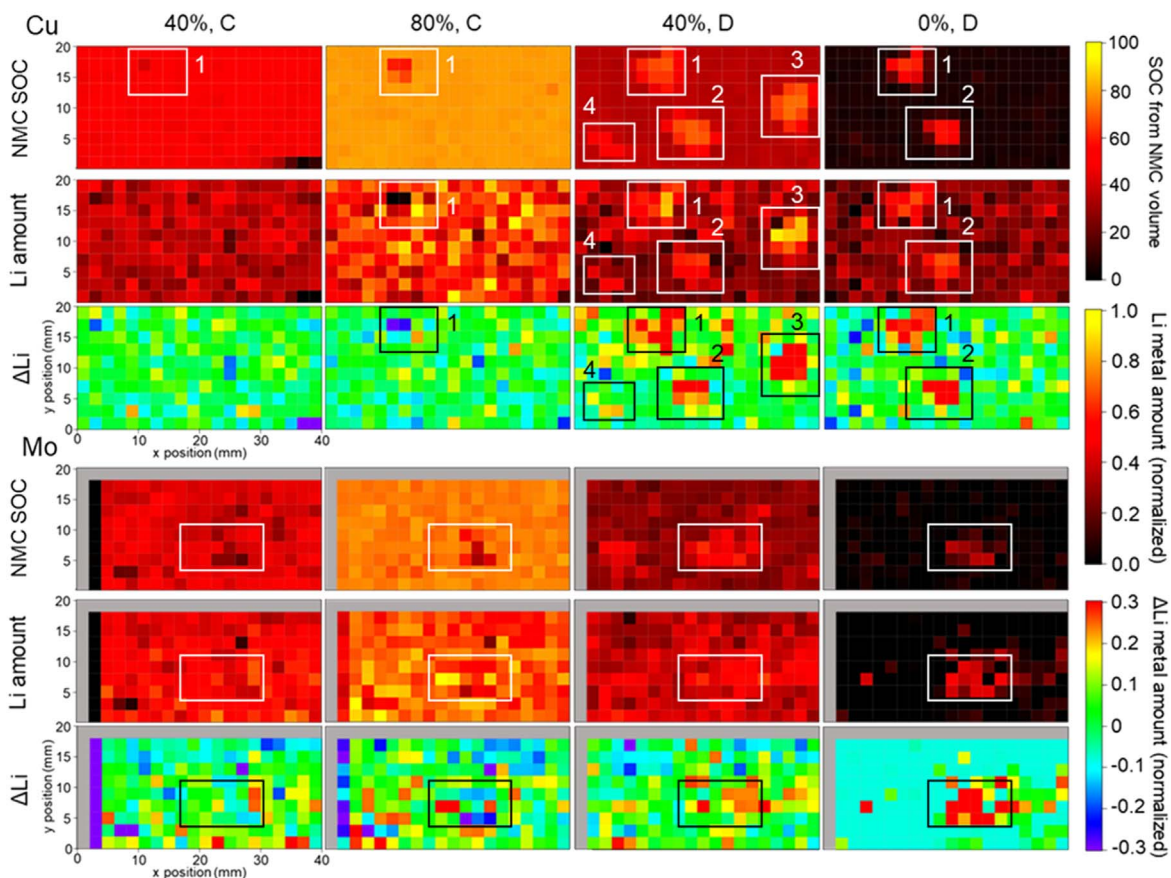


**Figure 5.** Lateral maps of the NMC SOC, the normalized Li amount, and the amount of Li relative to the mean ( $\Delta\text{Li}$ ) for the Cu/NMC cell (top) and the Mo/NMC cell (bottom) at each rest period during cycling. The apparent anomalous behavior at the bottom-right edge of the Cu/NMC cell and at the left edge of the Mo/NMC cell is attributed to refinement artifacts (due to edge effects) rather than to different electrochemical performance in these regions of the cell.

NMC622 pouch cells,<sup>22</sup> suggesting a common length scale for lateral transport in battery films. Regardless of the origin of the inhomogeneity, the mapping data indicates that the NMC SOC can serve as a reporter for inhomogeneity in Li plating and stripping that is more sensitive than the direct Li metal signal when the inhomogeneity is on a mm scale.

The mapping data clearly shows that the inhomogeneity observed during stripping is dynamic, with two of the Li metal spots (3 and 4) seen in the half-discharged (40% D) state disappearing as the cell is discharged to its minimum voltage (0% D). The other two spots (1 and 2) shrink in size, though with the lag in their SOC increasing to  $\sim 50\%$  relative to the baseline behavior in the cell. This suggests that not all dead Li is equivalent, with different spots having different barriers (overpotentials) for Li removal.

Even though severe inhomogeneity only develops during the first discharge of the Cu/NMC cell, there are potentially some hints during the preceding charge cycle about where the lagging spots will form. Although the Li deposition is quite homogeneous during the half-charged (40% C) map, there is one pixel which clearly lags relative to the rest of the cell and this pixel is found in the area associated with spot 1—a spot that persists all the way through to the end of discharge. In the fully charged (80% C) map, the single lagging pixel grows to encompass 4 pixels, and there is also a hint of a lagging pixel associated with spot 3. Similar behavior is also seen for the one large spot of dead Li that forms during the discharge of the Mo/NMC cell, as will be discussed in detail later.

When the behavior of the Mo/NMC cell is compared to that of the Cu/NMC cell, similarities and differences are observed. Much like the Cu/NMC cell, the Mo/NMC cell is more homogeneous during the first charge cycle than the first discharge cycle. However, the Mo/NMC cell is less homogeneous than the Cu/NMC cell during

both its charge and discharge segment, as can be seen in maps (Fig. 5), in the direct comparison of diffraction data (Fig. S5), and especially in the NMC SOC and Li amount histograms (Fig. S4). In addition to clearly showing up in the amount of Li (std. dev. from Gaussian fits to outlier-removed data is  $\sim 2\times$  larger than Cu/NMC), this larger inhomogeneity can also be clearly seen in the NMC SOC distributions ( $\sim 4\times$  larger), as reflected in the data of Tables SI–SIV. It is possible that the morphological differences between the Cu/NMC and the Mo/NMC cells are related to the different interactions of the Cu and Mo with Li metal. Mo is known to be more lithophobic than Cu,<sup>47</sup> which may result in the preferential deposition of Li on regions in which Li is already present and thus a more inhomogeneous distribution of Li metal during the first charge of the Mo/NMC cell. It has previously been shown that the crystallinity of Li metal affects electrochemical performance of batteries,<sup>48</sup> and it is certainly expected that the differences in Li deposition observed in the Cu/NMC and Mo/NMC cells will lead to different electrochemical performance.

Although the Mo/NMC histograms indicate a higher degree of overall inhomogeneity than the Cu/NMC cell, there is less of a tendency to form dead Li. Only a single macroscopic spot in which the Li removal is hindered is seen in the Li amount and  $\Delta\text{Li}$  maps. Although this spot is significantly larger than the ones seen in the Cu/NMC cell, its area is substantially less than the total Li area in the Cu/NMC cell at the half-discharged (40% D) state. However, the total amount of residual Li at the end of discharge (0% D) is similar to that for the Cu/NMC cell, as judged both by the spot areas and the discharge capacity of the cells.

The formation of the single region of lagging Li removal during the discharge of the Mo/NMC cell appears to have been presaged by slightly lagging Li deposition during the preceding charge segment.

This type of behavior was also seen in the Cu/NMC cell, indicating that it is generally relevant. Mechanistically, this suggests that the dead Li formation occurs at regions where the transport is worse than in the rest of the cell. One possibility is that the transport limitation is associated with regions on the metal surface that have a worse electronic conductivity, due to inhomogeneity in the foil thickness or due to chemical reactions that produce insulating SEI at the foil surface. However, this mechanism does not explain why the regions of inhomogeneity are so different in size and magnitude between the charge and discharge processes.

An alternate explanation that is more consistent with the observed behavior is that the transport limitation responsible for the formation of the spots is associated with the transport of ions in the electrolyte rather than with the transport of electrons in the metal foil. This could occur if the electrolyte is distributed unevenly in the cell due to wetting problems or the formation of gas bubbles. If this is the case, the large size of the spots (few mm) could be readily explained. Furthermore, this could drive the large differences in behavior between the charge and discharge segments. For the present electrolyte, the best ionic transport occurs when the  $\text{Li}^+$  concentration is around 1 M, with the ionic conductivity dropping both at lower concentrations (fewer mobile ions) and higher concentrations (increased viscosity which reduces the conductivity). During Li deposition in the charge segment, the concentration of Li in the electrolyte in the vicinity of the cathode increases (e.g., 1 M  $\rightarrow$  1.8 M), which has a small influence on ionic transport. In contrast, for Li stripping during the discharge segment, the same  $\text{Li}^+$  concentration decreases (e.g., 1 M  $\rightarrow$  0.2 M) in a manner that can cause large difference in ionic mobility. For example, if the amount of electrolyte is higher or lower than average, the local  $\text{Li}^+$  concentration maybe be higher (e.g., 0.8 M) or lower (e.g., 0.0 M) than the mean for the cell.

Conclusively resolving the mechanism responsible for the macroscopic regions of dead and/or lagging Li will require further experiments. If the effect is driven by the electrolyte concentration variations during cycling, it is expected that the lateral inhomogeneity during charge and discharge should be strongly dependent on the concentration of electrolyte, the type of electrolyte, the amount of the electrolyte, and the procedure used to load and evenly distribute the electrolyte. Furthermore, electrolyte concentration gradients are strongly rate dependent, and the observed behavior would be expected to thus also be highly rate dependent. In contrast, if the inhomogeneity is primarily determined by the metal of the substrate, then consistent behavior should be seen across multiple cells prepared using the same metal substrate, and substantial differences may occur when different types of metals are used. The inhomogeneity would in this case expected to be sensitive to the procedure used to clean the metal surface and might be sensitive to different sources of the metal (that differ in their crystallinity, preferred orientation, and/or thickness).

**Time-resolved studies of inhomogeneity (line scans).**—From the limited time resolution available from comparing maps, it was seen that the inactivation of “dead” Li is not so much an absolute as a relative process. Although all 4 spots of residual Li metal seen halfway through the discharge of the Cu/NMC cell represent regions in which the stripping of Li metal is greatly hindered relative to other regions of the cell, the map collected at the end of charge indicates that two of the Li-rich spots seen in the half-discharge (40% D) map disappear at the end of discharge (0% D). This indicates that the Li in those spots can be removed when a larger overpotential is applied or after eliminating competition with other regions from which Li can be more easily removed (i.e., due to the complete removal of Li from those regions). Complementary data with finer time resolution than the mapping data is needed to resolve the spatially-dependent kinetics of Li stripping and plating, and to understand how it varies as a function of position within the cell and as a function of SOC during cycling.

The need for spatially-resolved kinetic data during battery cycling was addressed by repeatedly collecting diffraction data over two lines of 5 points each during the galvanostatic cycling segments between the collection of maps (red regions in Fig. 2c). This data collection modality allowed the changes at each point to be followed with a time step of 10 min, corresponding to about 50 time steps across each charge and discharge segment of the battery. Two representative time series for the Cu/NMC cell are shown in Fig. 6 with their positions marked relative to a map of the NMC SOC at the end of discharge. Additionally, the full set of maps for the Cu/NMC and the Mo/NMC cells are provided in Figs. S7–S9, shown together with both the half-discharged (40% D) and fully-discharged (0% D) NMC SOC maps.

The agreement between the changes in the Li amount (blue) and the NMC SOC (red) during cycling are generally quite good, both at positions where the Li stripping is hindered (e.g., point 7) and at positions which it is unhindered (e.g., point 10). The direct sensitivity to the Li amount is lowest when the amount of Li metal is small, both due to the less intense diffraction signal and to the complete of overlap with the 101 diffraction peak of NMC that occurs when the NMC SOC is below  $\sim 25\%$ , as was illustrated in Fig. S2. This can cause challenges with the Li quantification at the beginning of charge and at the end of discharge, the two times when the Li amount is smallest. Conversely, the sensitivity to Li metal is highest when the local SOC is high. This is universally the case near at the end of the charge segment and at the beginning of the subsequent discharge segment. Additionally, for points where Li stripping is hindered, the regime of high sensitivity can persist for most or all of the discharge segment (e.g., points 3 and 7 in the Cu/NMC cell). The observation that Li metal persists through the end of discharge in macroscopic regions of the cell is thus robustly supported by both the line scan and the mapping data.

The mapping data suggests that there are four different regions in the cell with regard to the deposition and stripping of the data. Type 1 is normal pixels which show no lag during the deposition or stripping. Type 2 is pixels which exhibit normal Li plating but for which the Li stripping lags behind the cell as a whole yet still finishes by the end of discharge. Type 3 is pixels which exhibit normal Li plating but for which the Li stripping lags behind the cell as a whole and does not complete, even at the end of discharge. Type 4 is pixels which lag the cell as a whole both during Li plating and stripping, and where Li is not fully removed even at the end of discharge.

Six of the line scan pixels (1, 4, 5, 8–10) in the Cu/NMC cell behave in the average (Type 1) manner (Figs. 6 and S8), as do all of the line scan pixels in the Mo/NMC cell (Fig. S9). In these pixels, the behavior of the Li metal is generally indistinguishable from that of the NMC SOC within the sensitivity of the data. There are two noteworthy features in the data. First, the first discharge appears to progress more quickly than the first charge, as can be seen most clearly by comparing the behavior in the vicinity of the 40% C and 40% D map. Both the Li amount and the NMC SOC are lower at the 40% D state than in the 40% C state. If some portions of the cell are lagging during the Li stripping that occurs during discharge (e.g., Type 2, 3, and 4 pixels), then charge balance necessitates that the discharge process is accelerated for Type 1 pixels to compensate for this. Second, the amount of Li metal (and also the NMC SOC) almost invariably increases during the relaxation halfway through the discharge (40% D) for the Type 1 pixels. This also likely occurs as a consequence of interactions with the non-average pixels, whose behavior will be discussed next.

For the Cu/NMC cell, two pixels (2 and 6) exhibit Type 2 behavior, two pixels (3 and 7) exhibit Type 3 behavior, and no pixels exhibit Type 4 behavior. The line scan data confirm that the behavior of the Type 2 and Type 3 pixels during charging is indistinguishable from Type 1 pixels (Fig. S8). The data has been scaled so that the average amount of deposited Li on charging to 80% SOC corresponds to an Li amount of 0.8, and the measured amount of Li for

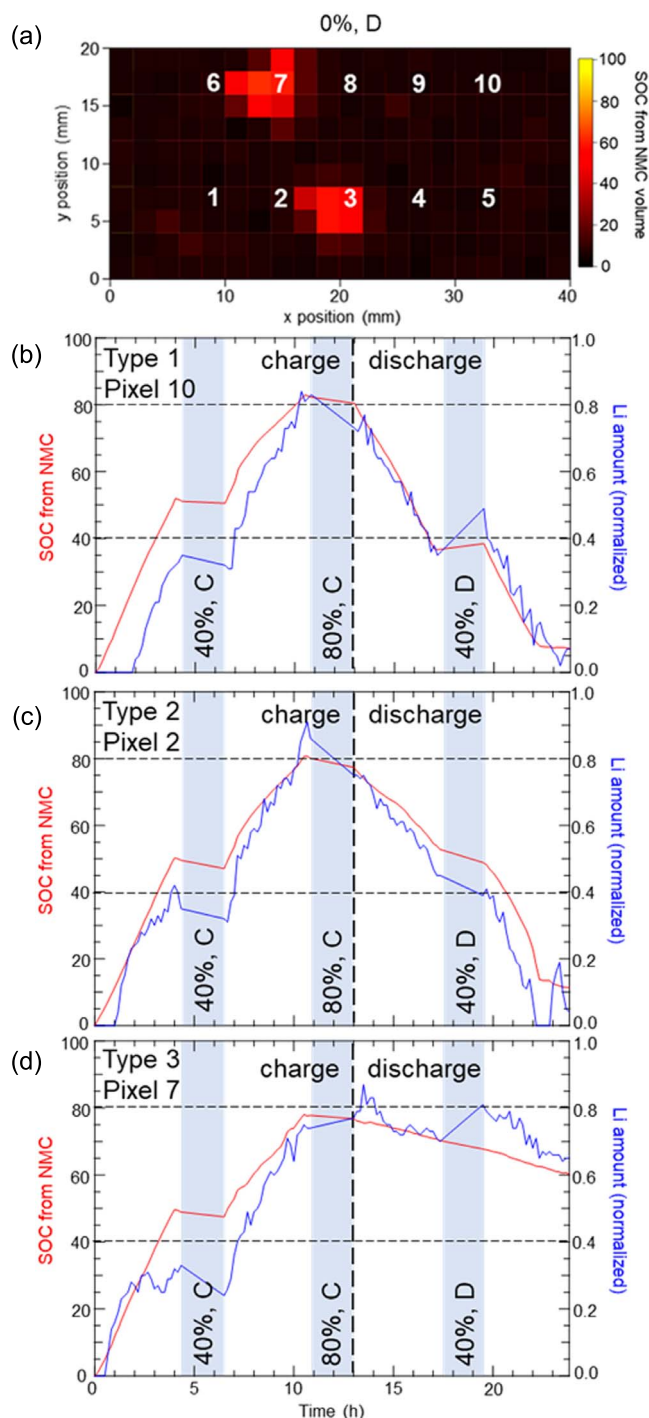


**Figure 6.** (a) The 10 pixel positions of the Cu/NMC cell at which line scan data were collected, shown superimposed on a map of the NMC SOC collected at the fully discharged (0% D) state. Time-dependent data for both NMC SOC (red) and Li amount (blue) as a function of time for (b) the Type 1 pixel 10, (c) the Type 2 pixel 2, and (d) the Type 3 pixel 7.

each of the 10 Cu/NMC pixels is very near this ideal amount. The Type 1 and Type 2 pixels achieve full Li removal at the end of discharge and thus have a Li amount of 0.0 at the end of discharge. In contrast, the Li amount for the Type 3 pixels is about 0.6 at the end of discharge, indicating that 75% of the plated Li remains.

There are very clear differences in the different types of pixels at the half-discharged (40% D) state. While the cell on average is expected to have a Li amount of 0.4, the Type 1 pixels have a Li

amount of 0.2–0.3 (leading), the Type 2 pixels have a Li amount of 0.4–0.5 (lagging), and the Type 3 pixels have a Li amount of 0.7 (severely lagging). For the Type 2 pixels (which lag during the beginning of discharge but finish by the end of discharge), the different rates during the first half and the second half of discharge can be clearly distinguished. For pixel 2, the local discharge rate at this position approximately doubles between the first half and the second half of discharge, as can be seen in the plots of both the Li amount and the NMC SOC. The rate difference for other Type 2 pixel, 6, is clearly seen though it is less severe.

The different pixel types of the Cu/NMC cell also behave differently during the 2 h relaxation halfway through discharge (40% D). For both Type 3 pixels, 3 and 7, the NMC SOC continues to decrease during relaxation at a rate similar to that during the times when the cell is being actively discharged in a manner. This contrasts with the behavior of the Type 1 pixels where the NMC amount remains constant or increases during this rest. This suggests that the large chemical potential inhomogeneity within the cells drives dynamic behavior that occurs over a long time scale during the rest, and that during this time the local potential in the Type 3 pixels is decreasing while those in the Type 1 pixels are increasing. The smooth decrease of the NMC SOC for the Type 3 pixel through both the discharge and relaxation periods suggest that these pixels are essentially unaffected by the applied potential, and that their changes are instead governed by longer range diffusional processes that mediate interactions with distant regions of the electrodes.

While the present data clearly demonstrate that synchrotron diffraction methods can have sensitivity to the plating and stripping of the small amounts of Li metal that occurs during the cycling of a single-layer Li-ion battery cell, the point-to-point scatter in the line scan data is on the order of 5%, almost two orders of magnitude higher than the sensitivity achieved for the NMC SOC. While the low-noise detector provided a critical enhancement in sensitivity, further improvements in sensitivity remain possible. Other beamlines could deliver a photon flux that is about an order of magnitude higher. Furthermore, the open configuration of the beamline resulted in an unusually long exposed path of the direct beam that resulted in a strong background from air scatter. While we are unaware of any existing beamline that is favorable in all of these parameters, a novel beamline designed to optimize performance in mapping experiments should be capable of achieving less than 1% uncertainty in the Li metal signal with shorter collection times of  $\sim 1$  s that would enable the rapid and precise tracking of Li metal during the cycling of next-generation high energy density batteries with sufficient sensitivity to enable the development of quantitative models that accurately predict the performance of novel cell designs.

## Conclusions

Using synchrotron X-ray diffraction methods, we have carried out the first *operando* experiments that directly track the deposition and stripping of Li metal during battery cycling using anode free Cu/NMC and Mo/NMC cells. Surprisingly, it was found that the initial deposition of Li metal is quite homogeneous while large heterogeneity first develops during the subsequent stripping of this Li. The inhomogeneity was much more pronounced in the Cu/NMC cell than in the Mo/NMC cell, though it has not yet been conclusively established if this is due to the influence of the metal substrate or the liquid electrolyte distribution. At selected points in each cell, the Li metal deposition and stripping was followed with fine temporal resolution. Different rates of Li utilization were observed between the charge and discharge segments, as well as between the first half and second half of discharge. It was universally observed that the ease of Li utilization was directly correlated with the degree of NMC utilization, resulting in a very strong spatial correlation in the behavior of the cathode and anode. Our novel characterization methods have provided new insights into the mechanisms associated with the formation of dead Li and into the dynamics that result from lateral inhomogeneity in Li metal batteries.

## Acknowledgments

This work was supported by the Assistant Secretary for Energy Efficiency and Renewable Energy, Office of Vehicle Technologies of the U.S. Department of Energy (DOE) through the Advanced Battery Materials Research (BMR) program and the Battery500 Consortium under Contract No. DE-SC0012704. The work of MRC was in part supported as a part of QuADS: Quantitative Analysis of Dynamic Structures National Science Foundation Research Traineeship Program, grant number NSF DGE 1922639. This research used resources of the Advanced Photon Source; a U.S. Department of Energy (DOE) Office of Science User Facility operated for the DOE Office of Science by Argonne National Laboratory under Contract No. DE-AC02-06CH11357. This manuscript has been authored by Battelle Energy Alliance, LLC under Contract No. DE-AC07-05ID14517 for Idaho National Laboratory with the U.S. Department of Energy. We greatly acknowledge the efforts of the entire staff at beamline 11-ID-C of the APS as well as the use of the dedicated eChem lab facility managed by K. Wiaderek.

## ORCID

Monty R. Cosby  <https://orcid.org/0000-0002-2951-7420>  
 Gia M. Carignan  <https://orcid.org/0000-0002-1152-3320>  
 Zhuo Li  <https://orcid.org/0000-0001-6388-3398>  
 Corey M. Efaw  <https://orcid.org/0000-0001-8996-0224>  
 Charles C. Dickerson  <https://orcid.org/0000-0002-8456-1563>  
 Liang Yin  <https://orcid.org/0000-0001-5396-782X>  
 Yang Ren  <https://orcid.org/0000-0001-9831-6035>  
 Bin Li  <https://orcid.org/0000-0002-2421-3153>  
 Eric J. Dufek  <https://orcid.org/0000-0003-4802-1997>  
 Peter G. Khalifah  <https://orcid.org/0000-0002-2216-0377>

## References

1. A. Masias, J. Marcicki, and W. A. Paxton, *ACS Energy Lett.*, **6**, 621 (2021).
2. Y. Wang, B. Liu, Q. Li, S. Cartmell, S. Ferrara, Z. D. Deng, and J. Xiao, *J. Power Sources*, **286**, 330 (2015).
3. S. Chu and A. Majumdar, *Nature*, **488**, 294 (2012).
4. J. Liu et al., *Nat. Energy*, **4**, 180 (2019).
5. Y. Meesala, A. Jena, H. Chang, and R.-S. Liu, *ACS Energy Lett.*, **2**, 2734 (2017).
6. J. Lang, L. Qi, Y. Luo, and H. Wu, *Energy Storage Mater.*, **7**, 115 (2017).
7. X.-B. Cheng, R. Zhang, C.-Z. Zhao, and Q. Zhang, *Chem. Rev.*, **117**, 10403 (2017).
8. J.-G. Zhang, W. Xu, and W. A. Henderson, *Lithium Metal Anodes and Rechargeable Lithium Metal Batteries* (Springer, Switzerland) (2017).
9. X. Zhang, Y. Yang, and Z. Zhou, *Chem. Soc. Rev.*, **49**, 3040 (2020).
10. X. Wu, K. Pan, M. Jia, Y. Ren, H. He, L. Zhang, and S. Zhang, *Green Energy Environ.*, **4**, 360 (2019).
11. K.-H. Chen, K. N. Wood, E. Kazyak, W. S. LePage, A. L. Davis, A. J. Sanchez, and N. P. Dasgupta, *J. Mater. Chem. A*, **5**, 11671 (2017).
12. K. N. Wood, E. Kazyak, A. F. Chadwick, K.-H. Chen, J.-G. Zhang, K. Thornton, and N. P. Dasgupta, *ACS Central Science*, **2**, 790 (2016).
13. B. L. Mehdi et al., *Nano Lett.*, **15**, 2168 (2015).
14. G. Bieker, M. Winter, and P. Bieker, *PCCP*, **17**, 8670 (2015).
15. C. Shen, G. H. Hu, L. Z. Cheong, S. Q. Huang, J. G. Zhang, and D. Y. Wang, *Small Methods*, **2** (2018).
16. Y. C. Hsieh, M. Leissing, S. Nowak, B. J. Hwang, M. Winter, and G. Brunklaus, *Cell Rep. Phys. Sci.*, **1**, 100139 (2020).
17. D. Tewari, S. P. Rangarajan, P. B. Balbuena, Y. Barsukov, and P. P. Mukherjee, *J. Phys. Chem. C*, **124**, 6502 (2020).
18. M. Zier, F. Scheiba, S. Oswald, J. Thomas, D. Goers, T. Scherer, M. Klose, H. Ehrenberg, and J. Eckert, *J. Power Sources*, **266**, 198 (2014).
19. S.-M. Bak, Z. Shadike, R. Lin, X. Yu, and X.-Q. Yang, *NPG Asia Mater.*, **10**, 563 (2018).
20. Z. Li et al., *Chem. Mater.*, **32**, 6358 (2020).
21. H. Liu, Z. Li, A. Grenier, G. E. Kamm, L. Yin, G. S. Mattei, M. R. Cosby, P. G. Khalifah, P. J. Chupas, and K. W. Chapman, *J. Appl. Crystallogr.*, **53**, 133 (2020).
22. G. S. Mattei, Z. Li, A. A. Corrao, C. Niu, Y. Zhang, B. Liaw, C. C. Dickerson, J. Xiao, E. J. Dufek, and P. G. Khalifah, *Chem. Mater.*, **33**, 2378 (2021).
23. P. P. Paul et al., *ACS Appl. Energy Mater.*, **4**, 11590 (2021).
24. L. G. Butler, E. H. Lehmann, and B. Schillinger, *Phys. Procedia*, **43**, 331 (2013).
25. F. Tang et al., *Small Methods*, **5**, 2100557 (2021).
26. P. Pietsch and V. Wood, *Annu. Rev. Mater. Res.*, **47**, 451 (2017).
27. F. F. Shi, A. Pei, A. Vailionis, J. Xie, B. F. Liu, J. Zhao, Y. J. Gong, and Y. Cui, *PNAS*, **114**, 12138 (2017).
28. G. Nazri and R. H. Muller, *J. Electrochem. Soc.*, **132**, 2050 (1985).
29. F. Lin et al., *Chem. Rev.*, **117**, 13123 (2017).
30. C. J. Niu et al., *Nat. Energy*, **6**, 723 (2021).
31. G. Ashiotis, A. Deschildre, Z. Nawaz, J. P. Wright, D. Karkoulis, F. E. Picca, and J. Kieffer, *J. Appl. Crystallogr.*, **48**, 510 (2015).
32. A. A. Coelho, *J. Appl. Crystallogr.*, **51**, 210 (2018).
33. J. Nelson, S. Misra, Y. Yang, A. Jackson, Y. Liu, H. Wang, H. Dai, J. C. Andrews, Y. Cui, and M. F. Toney, *JACS*, **134**, 6337 (2012).
34. S. Waluś, C. Barchasz, J.-F. Colin, J.-F. Martin, E. Elkaïm, J.-C. Leprêtre, and F. Alloin, *Chem. Commun.*, **49**, 7899 (2013).
35. L. de Biasi, A. Schiele, M. Roca-Ayats, G. Garcia, T. Brezesinski, P. Hartmann, and J. Janek, *Chem. Sus. Chem.*, **12**, 2240 (2019).
36. S. Kjeldgaard, S. Birgisson, A. G. Kielland, and B. B. Iversen, *J. Appl. Crystallogr.*, **51**, 1304 (2018).
37. C. D. Quilty, D. C. Bock, S. Yan, K. J. Takeuchi, E. S. Takeuchi, and A. C. Marschilok, *J. Phys. Chem. C*, **124**, 8119 (2020).
38. N. A. Canas, P. Einsiedel, O. T. Freitag, C. Heim, M. Steinhauer, D.-W. Park, and K. A. Friedrich, *Carbon*, **116**, 255 (2017).
39. X.-M. Zheng et al., *Nano Energy*, **77**, 105123 (2020).
40. H.-J. Liang, B.-H. Hou, W.-H. Li, Q.-L. Ning, X. Yang, Z.-Y. Gu, X.-J. Nie, G. Wang, and X.-L. Wu, *Energy Environ. Sci.*, **12**, 3575 (2019).
41. S. M. Bhaway et al., *ACS Nano*, **11**, 1443 (2017).
42. S. Schweidler, L. de Biasi, A. Schiele, P. Hartmann, T. Brezesinski, and J. R. Janek, *J. Phys. Chem. C*, **122**, 8829 (2018).
43. N. R. Geise, R. M. Kasse, J. Nelson Weker, H.-G. Steinrück, and M. F. Toney, *Chem. Mater.*, **33**, 7537 (2021).
44. J. Qian, B. D. Adams, J. Zheng, W. Xu, W. A. Henderson, J. Wang, M. E. Bowden, S. Xu, J. Hu, and J. G. Zhang, *Adv. Funct. Mater.*, **26**, 7094 (2016).
45. X. F. Wang et al., *Nano Lett.*, **17**, 7606 (2017).
46. C. C. Fang et al., *Nature*, **572**, 511 (2019).
47. V. Pande and V. Viswanathan, *ACS Energy Lett.*, **4**, 2952 (2019).
48. X. Wang et al., *Nat. Mater.*, **19**, 1339 (2020).